The Astrophysical Journal Letters, 940:L47 (9pp), 2022 December 1 https://doi.org/10.3847/2041-8213/aca0a1

Large Ion-neutral Drift Velocities and Plasma Heating in Partially Ionized Coronal Rain Blobs

David Martínez-Gómez[1,2], Ramón Oliver[3,4], Elena Khomenko[1,2], and Manuel Collados[1,2]
[1] Instituto de Astrofísica de Canarias, E-38205 La Laguna, Tenerife, Spain; dmartinez@iac.es
[2] Departamento de Astrofísica, Universidad de La Laguna, E-38205 La Laguna, Tenerife, Spain
[3] Departament de Física, Universitat de les Illes Balears, E-07122, Palma de Mallorca, Spain
[4] Institut d'Aplicacions Computacionals de Codi Comunitari (IAC3), Universitat de les Illes Balears, E-07122, Palma de Mallorca, Spain
Received 2022 September 16; revised 2022 November 4; accepted 2022 November 7; published 2022 November 30

Abstract

In this paper we present a numerical study of the dynamics of partially ionized coronal rain blobs. We use a two-fluid model to perform a high-resolution 2D simulation that takes into account the collisional interaction between the charged and neutral particles contained in the plasma. We follow the evolution of a cold plasma condensation as it falls through an isothermal vertically stratified atmosphere that represents the much hotter and lighter solar corona. We study the consequences of the different degrees of collisional coupling that are present in the system. On the one hand, we find that at the dense core of the blob there is a very strong coupling and the charged and neutral components of the plasma behave as a single fluid, with negligible drift velocities (of a few cm s^{-1}). On the other hand, at the edges of the blob the coupling is much weaker and larger drift velocities (of the order of 1 km s^{-1}) appear. In addition, frictional heating causes large increases of temperature at the transition layers between the blob and the corona. For the first time we show that such large drift velocities and temperature enhancements can develop as a consequence of ion-neutral decoupling associated to coronal rain dynamics. This can lead to enhanced emission coming from the plasma at the coronal rain-corona boundary, which possesses transition region temperature.

Unified Astronomy Thesaurus concepts: Solar physics (1476); Magnetohydrodynamical simulations (1966); Solar corona (1483); Plasma astrophysics (1261)

Supporting material: animation

1. Introduction

Plasma in the solar atmosphere may be found in a state of partial ionization. This means that it may contain a non-negligible amount of neutral particles which are not directly affected by the presence of magnetic fields. Neutral species have been detected, for instance, in solar prominences (see, e.g., Hirayama 1985), in chromospheric spicules (Pereira et al. 2016) or in coronal rain blobs (Antolinan & Rouppevander Voort 2012; Schad 2018).

From the theoretical point of view it is known that the dynamics of the ionized and the neutral species decouple at small enough spatial and temporal scales. This has been shown, for instance, by the works of Hillier (2019) and Popescu Braileanu et al. (2021a, 2021b), who used multi-fluid models to numerically study the development of the Kelvin–Helmholtz instability (KHI) and the Rayleigh–Taylor instability (RTI), respectively, in prominences. It has also been shown that the different behavior of the charged and neutral particles leads to the damping of waves and plasma heating due to the collisions between the various species (see, e.g., Leake et al. 2005; Zaqarashvili et al. 2011; Soler et al. 2013; Martínez-Gómez et al. 2018; Popescu Braileanu et al. 2019a)

However, the observational evidence regarding the different dynamics of charged and neutral species in the solar atmosphere is still scarce, mainly due to the requirements about temporal and spatial resolution. Khomenko et al. (2016) studied the Doppler shifts of the spectral lines He I 10830 Å and Ca II 8542 Å in observations of a solar prominence and deduced the existence of large ion-neutral drift velocities (of the order of several hundred m s^{-1}) in small-scale and short-lived transients. Anan et al. (2017) analyzed a larger set of spectral lines and also found differences in the Doppler velocities but they concluded that they were not caused by decoupling effects but were the result of observing motions originated at different regions of the prominence. Stellmacher & Wiehr (2017) performed observations of a quiescent prominence and systematically found an excess of ∼10% of the ion velocity over the neutral velocity. These results were later confirmed by Wiehr et al. (2019, 2021). Recent studies by S. J. González-Manrique et al. (2022, in preparation) and Zapiór et al. (2022) also point to the existence of large drift velocities (of up 1.7 km s^{-1}) in small regions of solar prominences. Regarding coronal rain observations, Ahn et al. (2014) compared the Doppler velocities computed from the spectral lines Hα and Ca II 8542 Å and found that they "matched well", although their results show that they are not completely identical.

Coronal rain is a very appropriate phenomenon to study the interaction between charged and neutrals species (Oliver et al. 2016). It involves a large range of ionization degree of the plasma, from the fully ionized case of the solar corona to the partially or weakly ionized condition of the falling blobs, which causes a large variation in the collisional coupling between the various species. However, most of the works on coronal rain dynamics have only considered the fully ionized case. This applies both to one-dimensional (e.g., Mendoza-Briceño et al. 2005; Müller et al. 2005;

Antolin et al. 2010; Mikic et al. 2013; Froment et al. 2018) and multi-dimensional numerical simulations (e.g., Mok et al. 2016; Xia et al. 2017; Kohutova et al. 2020; Li et al. 2022).

In the present work, we are interested in investigating the effects of that ion-neutral collisional interaction during the fall of cold condensations of plasma toward the solar surface. Therefore, we use a two-fluid model (Khomenko et al. 2014; Popescu Braileanu et al. 2019b) to perform high-resolution 2D simulations of the evolution of partially ionized coronal rain blobs. We focus on analyzing the existence of charged-neutral drift velocities and the plasma heating caused by the collisional friction. Then, we discuss observational consequences of these processes.

2. Methodology

2.1. Model

In this work, we assume that the plasma is composed of hydrogen only. Therefore, it contains three different kinds of particles: electrons, protons, and neutrals, which are denoted by the subscripts "e", "p", and "n", respectively. We also assume that the plasma fulfills the charge quasi-neutrality condition, so the number density of electrons and protons is the same, that is, $n_e = n_p$. Furthermore, a strong coupling between electrons and protons is considered, which allows to treat them together as a single charged fluid, denoted by the subscript "c". Then, the temporal evolution of this plasma is described by a two-fluid 2D model in which charged and neutral particles interact by means of elastic collisions.

The details of the full set of equations included in the two-fluid model can be found in Popescu Braileanu et al. (2019b) and Martínez-Gómez et al. (2021). Here we only show the most relevant terms for the present investigation, which are the momentum transfer and heating due to collisions, given by

$$\boldsymbol{R}_{cn} = \alpha \rho_c \rho_n (\boldsymbol{V}_n - \boldsymbol{V}_c) \tag{1}$$

and

$$Q_V = \alpha \rho_c \rho_n \frac{V_D^2}{2}, \tag{2}$$

respectively. In the previous expressions, the variables ρ_c, ρ_n, $\boldsymbol{V}_c$, and $\boldsymbol{V}_n$ represent the mass density of charges, the mass density of neutrals, the velocity of charges, and the velocity of neutrals, respectively. The parameter α is known as the collisional coupling coefficient and is given by

$$\alpha = \frac{\rho_e \nu_{en} + \rho_p \nu_{pn}}{\rho_n \rho_c}, \tag{3}$$

where ν_{en} and ν_{pn} are the electron-neutral and proton-neutral collision frequencies. The frequency of collisions between two different species "s" and "t" (when one of them is neutral) can be computed from the following expression (Draine 1986):

$$\nu_{st} = \frac{n_t m_t}{m_s + m_t} \sqrt{\frac{8 k_B}{\pi} \left(\frac{T_s}{m_s} + \frac{T_t}{m_t} \right)} \sigma_{st}. \tag{4}$$

Here, n_s, m_s, and T_s represent the number density, mass, and temperature of the species "s", respectively. The parameter k_B is the Boltzmann constant and σ_{st} is the collisional cross-section between the two species. We use the following values, taken from Leake et al. (2013): $\sigma_{pn} = 1.16 \times 10^{-18}\,\mathrm{m}^2$ and $\sigma_{en} = 10^{-19}\,\mathrm{m}^2$. We note that $n_c = n_e + n_p = 2n_p$, and the relation between the number and mass densities are $\rho_c = \rho_p + \rho_e = n_p m_p + n_e m_e \approx n_p m_p = n_c/2 m_p$ and $\rho_n = n_n m_n \approx n_n m_p$ (since for the case of hydrogen plasma $m_n \approx m_p$). Finally, the variable V_D is the modulus of the vector $\boldsymbol{V}_D$, which represents the drift velocity between the two fluids and is given by

$$\boldsymbol{V}_D = (V_{c,x} - V_{n,x},\, V_{c,z} - V_{n,z}) = (V_{D,x},\, V_{D,z}). \tag{5}$$

2.2. Numerical Setup

We numerically solve the two-fluid equations using the MANCHA-2F code (Popescu Braileanu et al. 2019b). In this code, the physical variables, $\boldsymbol{f}$, are treated as the sum of equilibrium values ($\boldsymbol{f}_{eq}$, which remain constant in time) and perturbation values ($\boldsymbol{f}_1$, which evolve with time and can be non-linear).

To simulate the fall of a partially ionized coronal rain blob we use as equilibrium a 2D isothermal vertically stratified atmosphere, with a temperature given by $T_0 = 2 \times 10^6\,\mathrm{K}$, a uniform vertical magnetic field given by $B_0 = 5\,\mathrm{G}$, and a plasma ionization degree given by $\chi_{c,eq} = \rho_{c,eq}/\rho_{T,eq} = 0.9$ (where $\rho_{T,eq} = \rho_{c,eq} + \rho_{n,eq}$). We note that in reality the equilibrium atmosphere representing the solar corona should be fully ionized (that is, $\chi_{c,eq} = 1$). However, due to numerical reasons (the fluid equations cannot be solved when $\rho_s(x, z) = 0$, since these variables appear in the denominators of several terms), we need to include a small fraction of neutrals in this environment. Thus, for our simulation we set the relative abundance of neutrals in the equilibrium state as $\chi_{n,eq} = \rho_{n,eq}/\rho_{T,eq} = 1 - \chi_{c,eq} = 0.1$.

As shown by Oliver et al. (2016), the condition of magneto-hydrostatic equilibrium leads to the following solutions from the two-fluid model:

$$\rho_{c,eq}(z) = \rho_{c,0} e^{-z/H_c},\ \rho_{n,eq}(z) = \rho_{n,0} e^{-z/H_n}, \tag{6}$$

$$P_{c,eq}(z) = P_{c,0} e^{-z/H_c},\ P_{n,eq}(z) = P_{n,0} e^{-z/H_n}, \tag{7}$$

where $P_{c,eq}$ and $P_{n,eq}$ are the equilibrium pressures of the charged and neutral fluids, respectively, and the following relations, corresponding to the values of density and pressure at the base of the corona ($z = 0$), are satisfied:

$$P_{c,0} = \frac{2\rho_{c,0} k_B T_0}{m_p},\ P_{n,0} = \frac{\rho_{n,0} k_B T_0}{m_p}. \tag{8}$$

The parameters H_c and H_n are the vertical scale heights of the charged and neutral fluids, respectively, and are computed as

$$H_c = \frac{2 k_B T_0}{m_p g} \text{ and } H_n = \frac{k_B T_0}{m_p g}. \tag{9}$$

For the simulation analyzed in the present work we use a value of $g = 273.98\,\mathrm{m\,s^{-2}}$ for the solar surface gravity, which produces vertical scale heights of $H_c \approx 120\,\mathrm{Mm}$ and $H_n \approx 60\,\mathrm{Mm}$. In addition, the densities at the coronal base are given by $\rho_{c,0} = \chi_{c,eq}\rho_{T,0}$ and $\rho_{n,0} = (1 - \chi_{c,eq})\rho_{T,0}$, where $\rho_{T,0} = 5 \times 10^{-12}\,\mathrm{kg\,m^{-3}}$ is the total density.

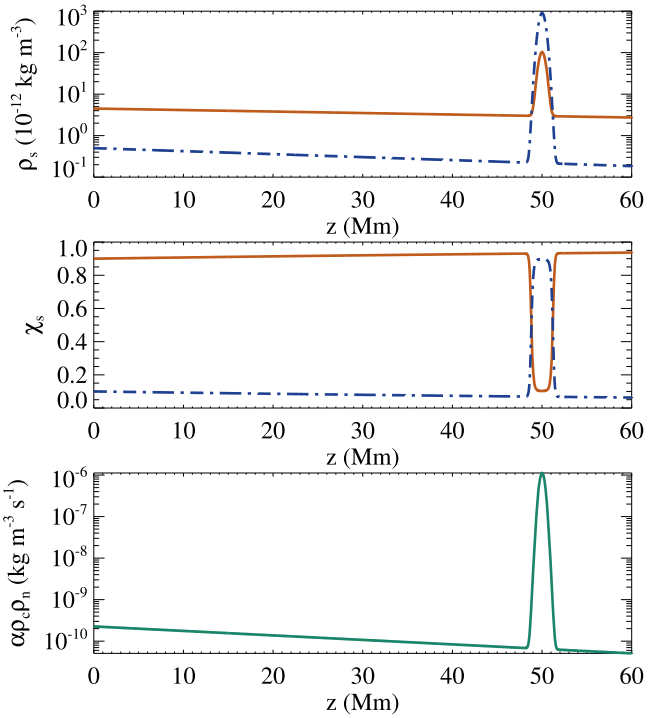

Figure 1. Sketch of the initial time of the simulation. Top and middle panels show the densities, ρ_s, and the relative abundances, χ_s, of the charged and neutral fluids, represented by orange solid lines and blue dashed-dotted lines, respectively. Bottom panel shows the coupling degree between the two fluids, given by the term $\alpha\rho_c\rho_n$.

We represent the coronal rain blob as a density perturbation for each species "s" given by

$$\rho_{s,1}(x, z) = \chi_s \rho_{b0} \exp\left[-\frac{(x - x_0)^2 + (z - z_0)^2}{\Delta^2}\right], \quad (10)$$

where $\chi_n = (1 - \chi_c)$, ρ_{b0} is the total density at the center of the blob, x_0 and z_0 are its initial coordinates, and Δ determines its width. For the present work we consider the following values of these parameters: $\rho_{b0} = 10^{-9}$ kg m^{-3}, $\chi_c = 0.1$ (the blob is weakly ionized), $x_0 = 0$, $z_0 = 50$ Mm, and $\Delta = 0.5$ Mm. The chosen value for ρ_{b0} produces a blob to corona density ratio of $\sim$300 at the height z_0. Taking into account this density ratio and the equilibrium in pressures, the temperature of the blob is $T_{b0} \approx 7000$ K, which corresponds to a typically chromospheric temperature.

Therefore, at the initial time of the simulation, the density profiles are given by the sum of Equations (6) and (10), as shown in the top panel of Figure 1 (which corresponds to vertical cuts of densities at the position $x = 0$). In addition, the middle panel of Figure 1 shows the relative abundances of the two fluids, χ_c and χ_n, and the bottom panel shows the collisional coupling between the two fluids (represented by the factor $\alpha\rho_c\rho_n$) as a function of height.

Finally, we consider a physical domain that extends from -5 to 5 Mm in the horizontal direction and from -20 to 80 Mm in the vertical direction. We represent it with a numerical mesh of $10^3 \times 10^4$ points, which corresponds to a resolution of 10 km. We apply periodic boundary conditions in the horizontal direction and Perfectly Matched Layers (PML; Berenger 1994; Parchevskyand & Kosovichev 2009) in the vertical direction.

3. Results

Once the temporal evolution starts, the partially ionized blob begins to fall toward the lower boundary under the action of gravity. As described by Oliver et al. (2014) the motion followed by the blob does not correspond to what is expected for a freefall. This is due to the development of a pressure gradient that opposes the gravity force and slows down the plasma. The falling speed strongly depends on the blob to corona density ratio, with a larger density leading to a faster fall since a larger pressure gradient is required to balance the gravity force. Then, in agreement with the results from Martínez-Gómez et al. (2020), the horizontal variation of the density leads to a deformation of the blob because its lighter regions fall slower than the denser ones. From its initial Gaussian profile, given by Equation (10), the blob turns into an elongated V-shape as time advances. This deformation can be checked by looking at the density contours represented in Figure 2 (see also the animation accompanying this figure).

The charged fluid is directly affected by the magnetic field while the neutral one is not, which in principle would lead to different dynamics for each fluid. Another reason for the different dynamics of the two fluids would be that their blob to corona density ratio and their vertical scale heights are different. However, in the simulation studied here both components of the plasma show an almost identical behavior due to the existence of the collisional coupling. Broadly speaking, both follow the evolution described in the previous paragraph, although important differences between them can be found. For instance, the color maps on panels (a) and (b) of Figure 2 show the x-component and the z-component of the drift velocity between the two fluids, respectively, at a given time of the simulation. In the central and denser part of the blob, the drift velocity is very small, of the order of centimeters per second, in agreement with the results from the 1D study of Oliver et al. (2016). This is a consequence of a very strong collisional coupling caused by a very large total density. Nonetheless, much larger drift velocities, of the order of kilometers per second are also present, which means that there are regions where the charged-neutral interaction is not as strong as in the core of the blob. We see that these large drift velocities appear mainly at the wings of the blob and at its external layers. The presence of such differences in the velocities of the two fluids is accompanied by heating of the plasma, as shown on panel (c) of Figure 2, where we represent the frictional heating term given by Equation (2).

An interesting feature of the evolution of the falling blob is that the horizontal drift velocities are consistently larger than the vertical ones, as it can be checked by comparing the panels (a) and (b) of Figure 2. This fact can be explained as follows. Martínez-Gómez et al. (2020) showed that, as a fully ionized plasma blob falls, the gas pressure tends to produce a horizontal expansion, which would lead to a large deformation of the falling condensation. However, in the presence of a relatively strong magnetic field there is a magnetic tension that almost perfectly balances the effect of the pressure. In the case of a partially ionized plasma, only the charged component is directly affected by this magnetic tension and a noticeable horizontal expansion of the neutral component is only prevented by the effect of the collisional coupling. Conversely, the influence of the magnetic field on the vertical motion is almost negligible, so there is not such a difference in the forces affecting each fluid. Therefore, in the horizontal direction a

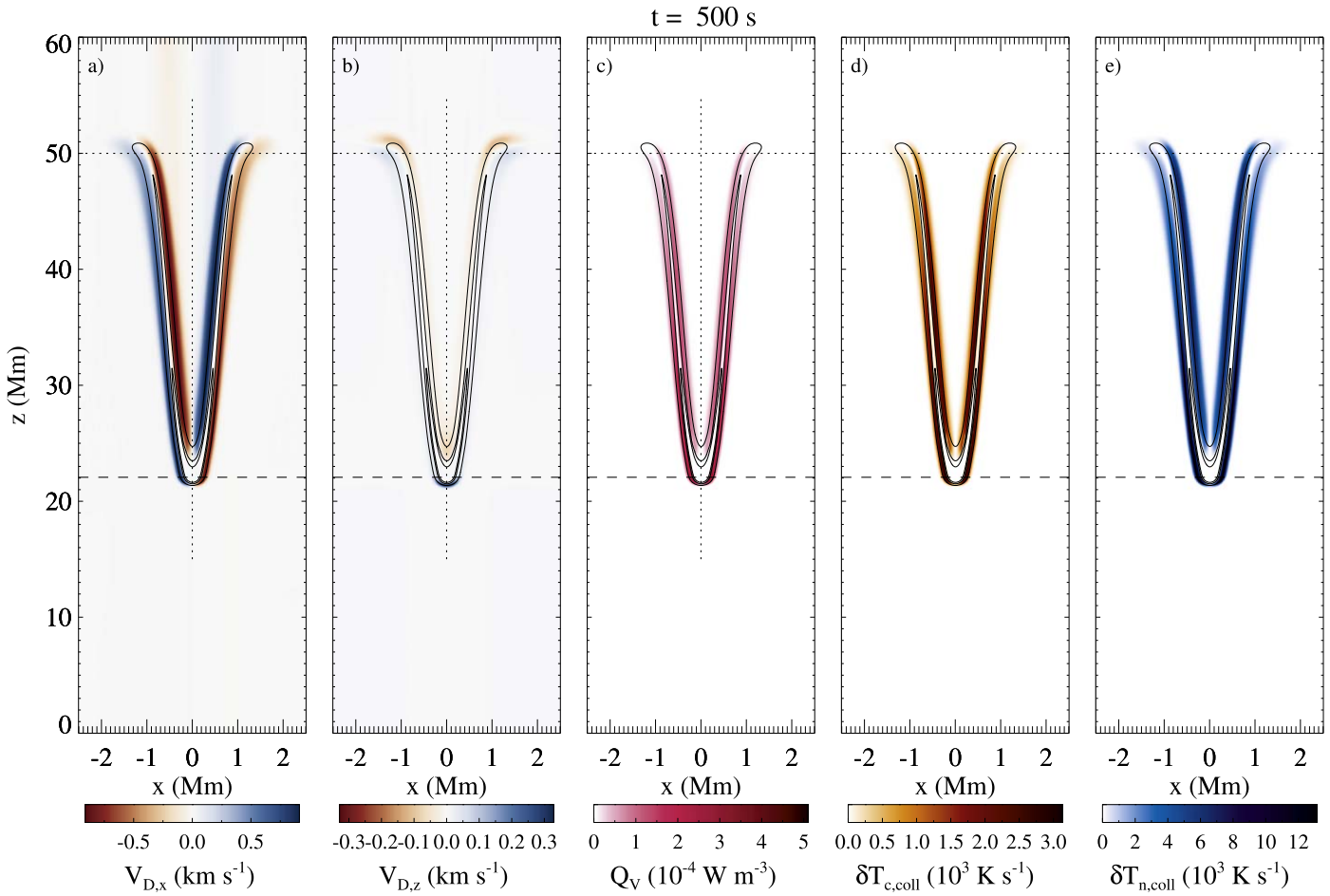

Figure 2. Snapshot of the simulation of a falling coronal rain blob. (a) and (b): color maps of the x-component and z-component of the drift velocity, $V_{D,x}$ and $V_{D,z}$, respectively; (c): color map of the frictional heating, Q_V; (d) and (e): color maps of the temperature variations of the charged and the neutral fluid, respectively, caused by the frictional heating represented in (c). Black solid lines represent density contours of the neutral fluid. A vertical dotted line has been drawn at $x = 0$ and two horizontal dashed and dotted lines have been drawn at the maximum density and initial blob positions, respectively. (An animation of this figure is available online. The animation runs from $t = 10$ s to $t = 660$ s. The real-time animation duration is 11 s. The animation shows the evolution of the variables presented in the figure and how the initial Gaussian profile of the blob, given by Equation (10) develops into a V-shape as the plasma falls down.)

(An animation of this figure is available.)

large drift velocity is required to play a similar role to the magnetic tension of the fully ionized scenario, while in the vertical direction smaller drift velocities appear.

To get a more detailed picture of the evolution of the drift velocities and heating profiles, we show in Figure 3 horizontal and vertical cuts of these variables at different times of the simulation. The horizontal cuts, shown in the top panels, are computed at the height where the maximum of density is located at each moment, represented in Figure 2 by the horizontal black dashed lines (the horizontal dotted lines in Figure 2 show the starting position of the blob). The position of the vertical cuts (bottom panels of Figure 3) is shown in Figure 2 as dotted black lines. We see in the horizontal cuts that the drift velocities and heating profiles (left and right panels, respectively) share their main features: very small values are found at the center ($x = 0$); then, there is a large increase in magnitude as we move toward the wings of the falling blob; and, finally, their magnitudes decrease again in the plasma of the external corona. As a consequence of the blob deformation during its fall, these horizontal cuts display two maxima that become less separated with time. The vertical cuts show that the larger drift velocities and heating appear at the front and the back of the blob, while they are negligible at its center. Figure 3 also reveals that the magnitudes of the drift velocities and the frictional heating increase with time. This behavior is discussed below.

The increase of the frictional heating with time is shown in the top panel of Figure 4, where we represent the spatial average of this quantity as a function of time (the spatial averages are performed over the computational domain given by $-2.5\,\mathrm{Mm} < \times < 2.5\,\mathrm{Mm}$ and $0 < z < 60\,\mathrm{Mm}$, that is, the domain represented in Figure 2). The main reason for this increase is that in this simulation the blob is still gaining speed as it falls. The pressure gradient has not been able to fully balance the gravity force yet and the blob has not reached the constant speed phase described in Oliver et al. (2014) and Martínez-Gómez et al. (2020). This behavior of the falling speed is represented in the middle panel of Figure 4. In addition, in the bottom panel of Figure 4 we compare the temporal evolution of the maximum value of the drift velocity (green solid line) and the spatially averaged drift velocity, $\langle V_D \rangle$ (dotted line). On the one hand, we see that the maximum drift velocity is of the order of 1 km s^{-1}, which is approximately 1% of the falling speed, while the spatially averaged drift velocity at the end of the simulation is of the order of 100 m s^{-1}. On the other hand, we see that the maximum of the drift velocity

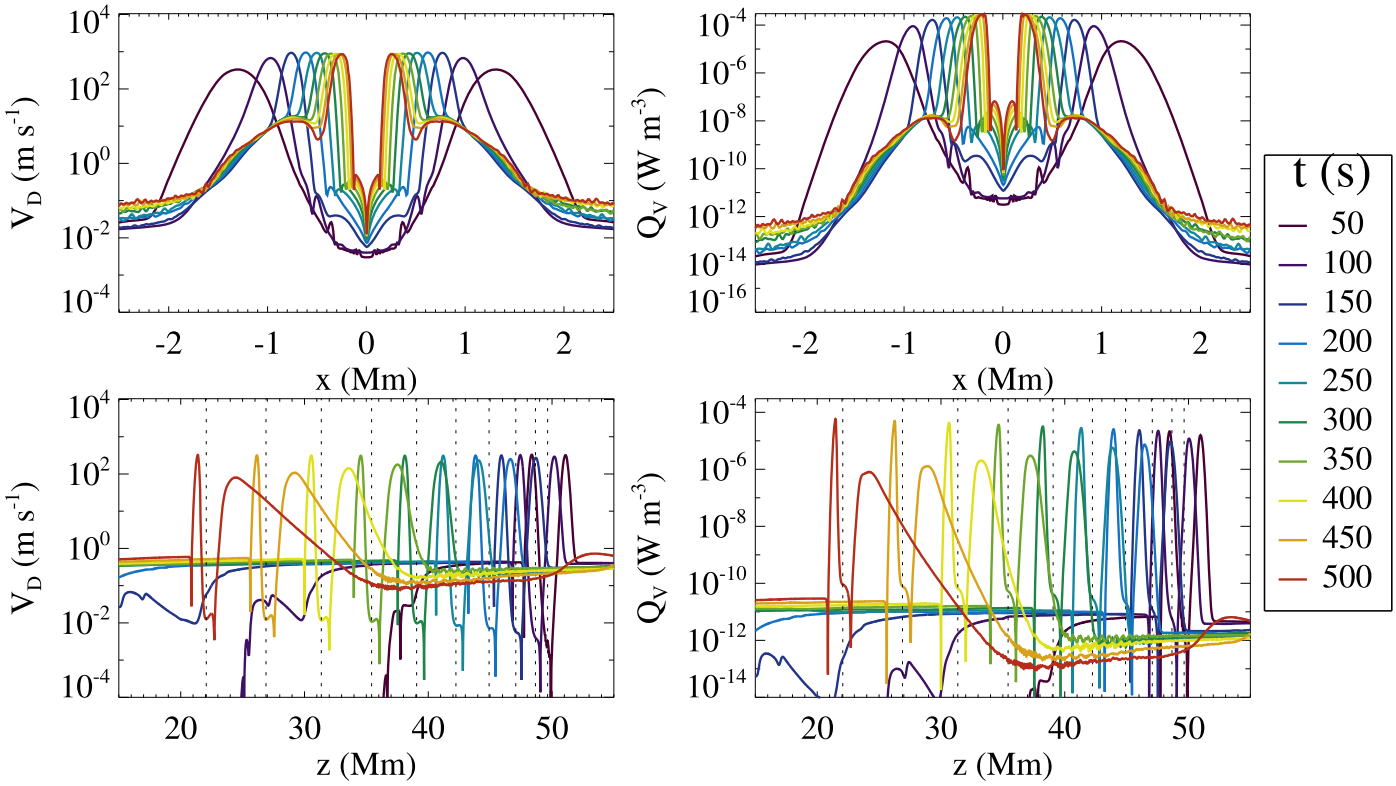

Figure 3. Top and bottom panels show horizontal and vertical cuts, respectively, of the absolute value of the drift velocity (left) and the heating term (right). Each line color corresponds to a different time of the simulation. Vertical dotted lines in the bottom panels mark the position of the density peak at each time.

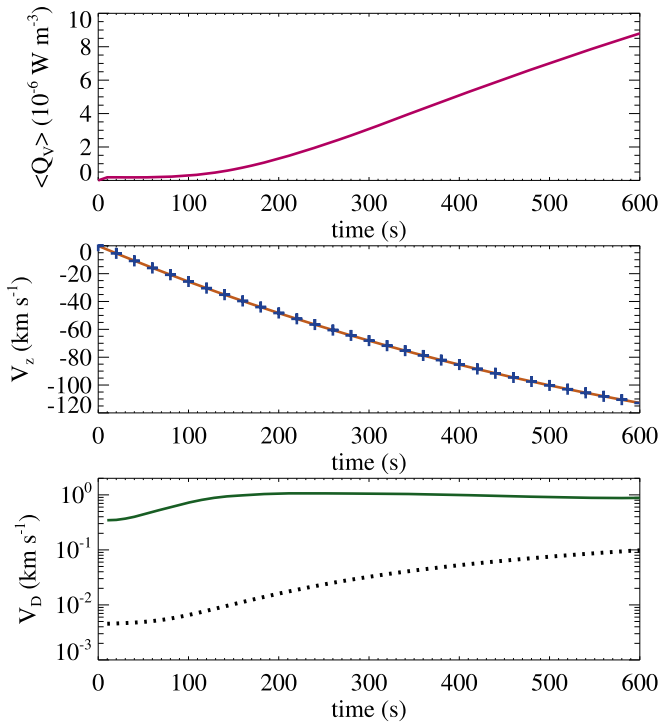

Figure 4. Top panel shows the spatially averaged value of the heating term, $\langle Q_V \rangle$, as a function of time. The solid orange line and the blue crosses in the middle panel show the falling speed of the density peak of the charged and the neutral fluid, respectively, as a function of time. The bottom panel shows the maximum of the drift velocity (green solid lines) and the spatially averaged drift velocity (black dotted line) as a function of time.

saturates around the time $t \sim 200$ s, while the spatially averaged values keeps increasing with time. This increase is caused by a larger fraction of the domain reaching the saturation value of drift velocity as time advances, and leads to the build-up of $\langle Q_V \rangle$.

After analyzing the evolution of the drift velocities and the frictional heating, it is also interesting to investigate the variations of temperature related to the charged-neutral interaction. As shown by Martínez-Gómez et al. (2021), the frictional heating produces an increase of temperature of each fluid given by the following expressions:

$$\delta T_{\rm c,coll} = \frac{(\gamma - 1)}{n_{\rm c} k_{\rm B}} Q_V \quad \text{and} \quad \delta T_{\rm n,coll} = \frac{(\gamma - 1)}{n_{\rm n} k_{\rm B}} Q_V, \qquad (11)$$

where $\gamma = 5/3$ is the adiabatic constant. These expressions give a direct proportionality between the friction heating and the temperature increase of both species.

We show in panels (d) and (e) of Figure 2 color maps of the variables $\delta T_{\rm c,coll}$ and $\delta T_{\rm n,coll}$, respectively, together with neutral density contours. As expected, the largest variations of temperature are located at the areas with the largest values of Q_V. To understand the temperature increase of both species, we compare the profiles of the variations of temperature with those of the densities and the relative abundances ($\chi_{\rm c}$ and $\chi_{\rm n}$). In the same way as in Figure 3 for the cases of the drift velocities and the heating term, we show in Figure 5 horizontal cuts of the temperature variations (top panels), of the densities (middle panels), and of the relative abundances (bottom panels) at selected times of the simulation. Results for the charged and the neutral fluids are shown in the left and right panels, respectively. We see that the profiles of the temperature variations are similar to those of the

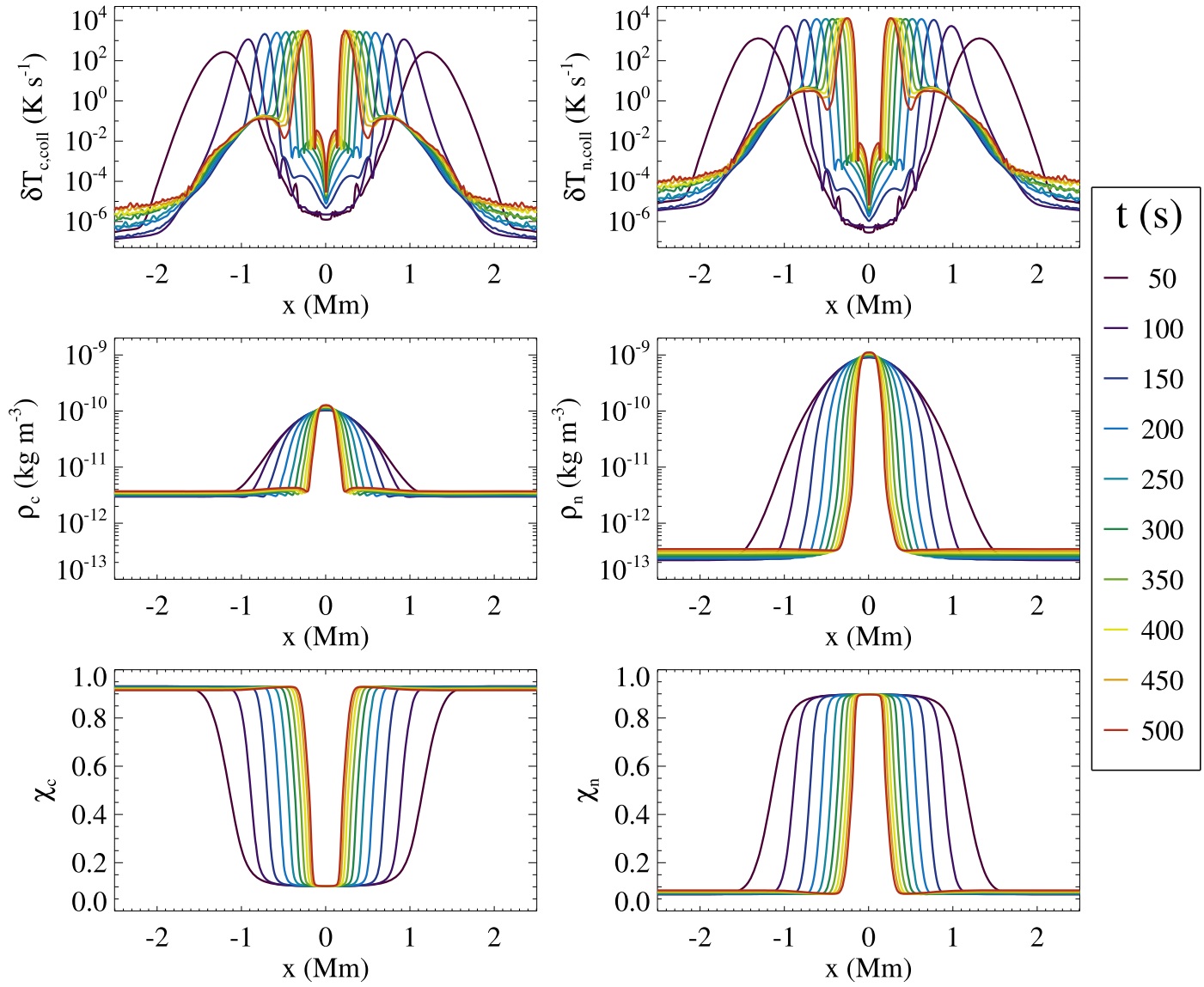

Figure 5. Horizontal cuts of the temperature variations caused by charged-neutral collision (top panels), densities (middle panels) and relative abundances, χ_c and χ_n (bottom panels). Left panels show the results for the charged fluid and right panels show the results for the neutral fluid. Each line color corresponds to a different time of the simulation.

frictional heating shown in Figure 3: the larger values appear at the wings of the blob while the variations of temperature at the core of the blob are negligible. In addition, at every step of the simulation the maximum values of $\delta T_{\rm n,coll}$ are larger than those of $\delta T_{\rm c,coll}$, in agreement with the results presented in Figure 2. Then, the comparison with the density and abundance profiles shows that the regions of larger values of $\delta T_{\rm c,coll}$ and $\delta T_{\rm n,coll}$ correspond to regions with larger values of the ionization degree, that is, where the density of neutrals is much smaller than the density of charged particles ($\chi_{\rm n} \ll \chi_{\rm c}$). Finally, Figure 5 clearly shows that the most important increases of temperature due to the collisional interaction occur at the transition layer between the blob and the coronal plasma.

Finally, to complement this analysis of the heating and temperature variations of the plasma, we refer the reader to the Appendix, where we present a comparison between the frictional heating due to collisions and the adiabatic heating caused by the compression of the plasma as the blob falls through the corona.

4. Discussion and Conclusions

In this paper we have used a two-fluid model to simulate the fall of a partially ionized coronal rain blob. Our results show the existence of several regimes of interaction between the charged and neutral species contained in the plasma. On the one hand, due to the large densities at the core of the blob, there is a very strong collisional coupling and, therefore, the dynamics of this region is well described by single-fluid model (Oliver et al. 2016; Martínez-Gómez et al. 2020). On the other hand, as we move toward the external layers of the cold condensation, the density decreases and the coupling due to collisions becomes weaker. This is specially evident in the thin region that connects the weakly ionized blob with the fully ionized coronal plasma. The simulation analyzed here shows that, as a consequence of this weak coupling, large drift velocities between the charged and the neutral species appear, accompanied by heating of the plasma due to the collisional friction. This implies that there is no longer a single-fluid dynamics and that the use of a multi-fluid description is

required. To the best of our knowledge, this is first time that the existence of large ion-neutral velocity drifts in coronal rain events is reported, either in a numerical or in an observational work.

The maximum drift velocities found in our simulation are of the order of $1\,\mathrm{km\,s^{-1}}$. Similar values have been reported in other studies of partially ionized plasmas in different scenarios of the solar atmosphere, such as numerical simulations of the RTI (Popescu Braileanu et al. 2021b) or observations of solar prominences (Khomenko et al. 2016; Anan et al. 2017; Stellmacher & Wiehr 2017; Wiehr et al. 2019, 2021; S. J. González-Manrique et al. 2022, in preparation; Zapiór et al. 2022). Therefore, the combination of numerical simulations and observations offers a coherent picture of the evolution of the partially ionized plasmas in coronal structures such as prominences or coronal rain blobs: while the various components of the plasma approximately behave as a single fluid in the central and denser regions of these structures, important differences in the motions of the charged and the neutral species appear at the edges. Coronal rain drops are expected to be essentially optically thin, which would facilitate measuring velocities of different species. An observational confirmation of the drift velocities predicted by the present numerical study could be obtained through a dedicated campaign on a large-aperture telescope. It should be taken into account that, according to the results presented in Figure 2, it would be easier to detect the drifts in the horizontal motions of the plasma than along the direction of the fall of the blobs.

In our simulation we have found that the charged-neutral interaction causes increases of temperature of up to 10^3–$10^4\,\mathrm{K\,s^{-1}}$. In principle, these values seem extremely high but we remind that they occur at the blob to corona transition regions, where the initial temperature of the plasma is already of the order of 10^5–10^6 K. Moreover, the magnitude of the blob temperature and its variation might not be accurate for a realistic scenario, since in our model we have not followed the full blob formation cycle (Mikic et al. 2013; Kohutova et al. 2020; Li et al. 2022) driven by the thermal instability (Parker 1953; Field 1965). For this research, we have resorted to the ideal equation of state and we have neglected non-adiabatic processes such as thermal conduction, radiative losses or ionization and recombination. Furthermore, we have started the simulation with an already formed blob which is included as a density perturbation superimposed to the background atmosphere. In this way, the initial temperature of the blob is directly related to the density ratio between the perturbation and the equilibrium.

Thus, our findings regarding the heating process should be taken as a qualitative description instead of a quantitative one. Nevertheless, from this qualitative point of view we may argue that the frictional heating obtained in the simulation would have associated observational signatures. It would produce an enhanced emission coming from the blob to corona transition region when observed in spectral lines associated to hot plasma, which might explain the brightenings detected in coronal rain observations (see, e.g., Antolin 2020). This statement could be checked by performing forward modeling (see, e.g., Antolin et al. 2022; Antolin & Froment 2022) and comparing the results from simulations of a partially ionized plasma with those for the fully ionized case. However, this task is out of the scope of the present paper and is left for a follow-up research. Finally, to get a more accurate description of this phenomenon it is important to include in future works the non-adiabatic effects that have not been considered here. For instance, the processes of ionization and recombination can enhance the density of the charged fluid in a thin layer around the cold blob, due to the ionization of the neutrals at the interface between the blob and the corona (Popescu Braileanu et al. 2021b). As a consequence, an enhanced emission could be produced at this layer in a similar way as it has been detected in prominence to corona transition regions (Berger et al. 2017). In addition, as shown by Zhang et al. (2021), ionization and recombination generate larger decoupling between charges and neutrals, which would result in larger drift velocities and collisional heating.

This work was supported by the European Research Council through the Consolidator Grant ERC-2017-CoG-771310-PI2FA. This publication is part of the R + D + i project PID2020-112791GB-I00, financed by MCIN/AEI/10.13039/501100011033. D.M. also acknowledges support from the Spanish Ministry of Science and Innovation through the grant CEX2019-000920-S of the Severo Ochoa Program. We thankfully acknowledge the technical expertise and assistance provided by the Spanish Supercomputing Network (Red Española de Supercomputacion), as well as the computer resources used: the LaPalma Supercomputer, located at the Instituto de Astrofisica de Canarias. We also would like to thank the anonymous referee for providing very useful comments.

Appendix
Comparison of Frictional and Adiabatic Heating

In the main text of this work we have only paid attention to the non-ideal process of plasma heating due to collisions between the charged and the neutral particles. However, our model also contains an ideal mechanism that plays a role in the variations of temperature of the two fluids: the adiabatic heating (and cooling) related to compressions (and expansions) of the plasma. In the present section we study how the ideal and non-ideal heating processes compare to each other.

From Martínez-Gómez et al. (2021), the equations that describe the temporal evolution of the internal energy of the charged and the neutral fluids, e_c and e_n, respectively, are given (in the absence of Joule heating) by

$$\frac{\partial e_c}{\partial t} + \nabla \cdot (e_c \boldsymbol{V}_c) + P_c \nabla \cdot \boldsymbol{V}_c = Q_T + Q_V \tag{A1}$$

and

$$\frac{\partial e_n}{\partial t} + \nabla \cdot (e_n \boldsymbol{V}_n) + P_n \nabla \cdot \boldsymbol{V}_n = -Q_T + Q_V, \tag{A2}$$

where Q_T is the term of thermal exchange due to collisions, which depends on the difference of the temperatures of the two fluids and has the main effect of keeping the two components of the plasma at the same temperature. Neglecting the effect of this term, Equations (A1) and (A2) can be written as

$$\frac{\partial e_c}{\partial t} + \nabla \cdot (e_c \boldsymbol{V}_c) = Q_{\mathrm{ad},c} + Q_V \tag{A3}$$

and

$$\frac{\partial e_n}{\partial t} + \nabla \cdot (e_n \boldsymbol{V}_n) = Q_{ad,n} + Q_V, \tag{A4}$$

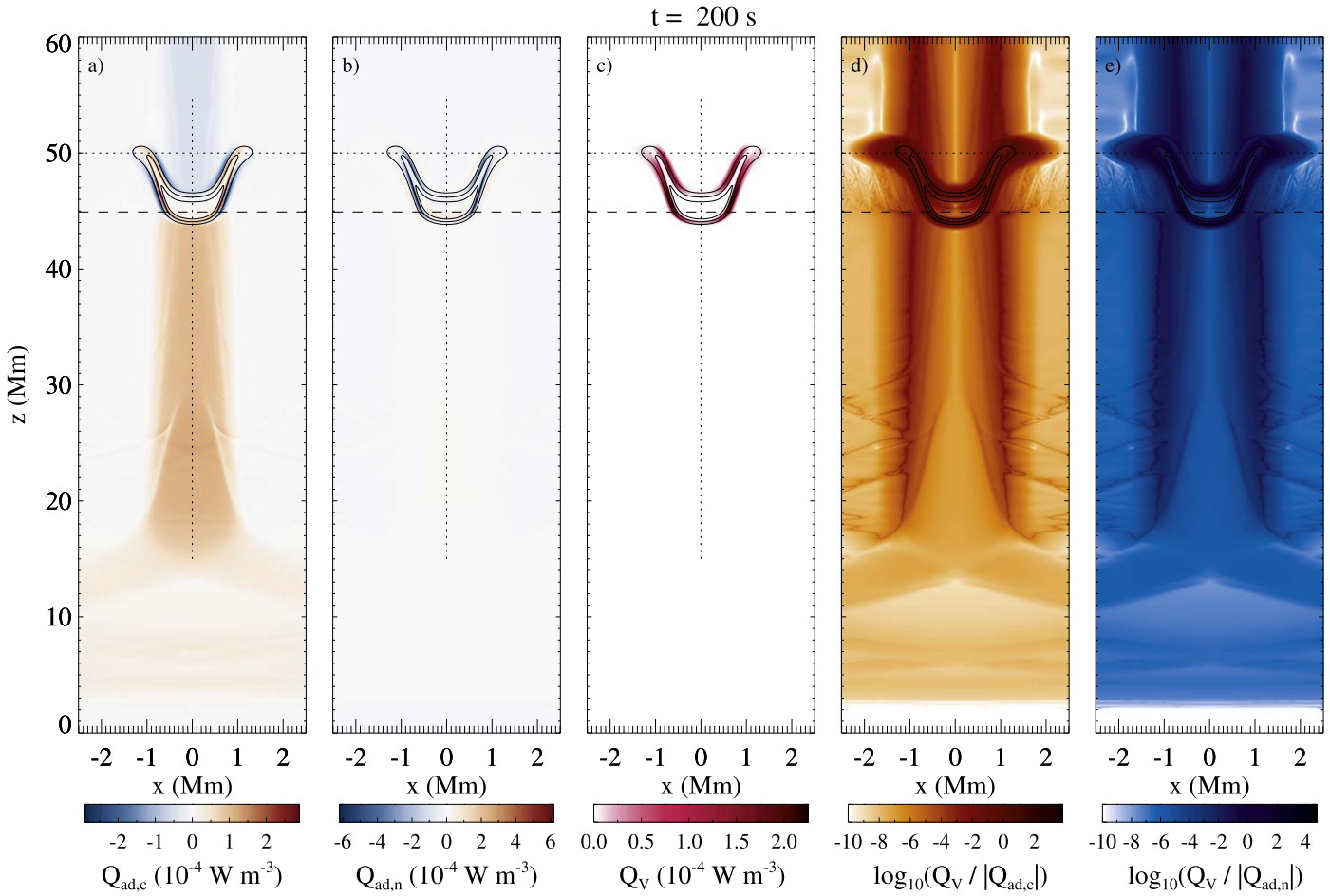

Figure A1. Comparison between adiabatic and frictional heatings. panels (a) and (b) represent the adiabatic variation of internal energy of the charged and the neutral fluids, $Q_{ad,c}$ and $Q_{ad,n}$, respectively. Panel (c) shows the frictional heating due to collisions. panels (d) and (e) represent the ratios between the frictional heating and the absolute values of $Q_{ad,c}$ and $Q_{ad,n}$, respectively.

where

$$Q_{ad,c} \equiv -P_c \nabla \cdot \boldsymbol{V}_c \quad \text{and} \quad Q_{ad,n} \equiv -P_n \nabla \cdot \boldsymbol{V}_n \tag{A5}$$

are the variations of the internal energy of each fluid related to the expansions and compressions of the plasma, that is, the adiabatic cooling and adiabatic heating, respectively.

We present in Figure A1 the computations of the different kinds of heating terms for a given snapshot of the simulation analyzed in the main body of the paper. Panel (a) shows that, as the blob falls, the charged fluid below it increases its temperature because there is a compression caused by an increase of the pressure (see Martínez-Gómez et al. 2020). The opposite situation occurs above the falling blob: the pressure reduces and, consequently, the plasma cools down. The same behavior takes place in the neutral fluid, although it cannot be clearly seen in panel *b)* of Figure A1 because of the large difference in the pressure of neutrals between the interior of the blob and the corona. Nevertheless, panels (a) and (b) show that there large variations of temperature of the two fluids in the borders of the blob. The comparison with the frictional heating shown in panel (c) reveals that the adiabatic and the frictional heatings are of the same order of magnitude around the blob but, more important, they do not take place at the same locations. Thus, there are regions of the domain where the only contribution to plasma heating comes from the charged-neutral collisions. This fact can also be checked by looking at the ratios $\log_{10}(Q_V/|Q_{ad,c}|)$ and $\log_{10}(Q_V/|Q_{ad,n}|)$ shown in panels (d) and (e), where the darker colors correspond to areas in which the frictional heating dominates over the adiabatic mechanism (we note here that the color maps of these two panels are saturated in the lower limit of ratios, that is, for values below -10).

Finally, Figure A2 represents the maximum values of the heating terms as functions of time. To compute these values, we have considered the domain represented in Figure A1. We see that in general the adiabatic heating of the charged fluid is larger than the one for the neutral fluid and the frictional heating. However, the three terms are of the same order. In addition, we know from Figure A1 that the largest values of the ratios $Q_V/|Q_{ad,c}|$ and $Q_V/|Q_{ad,n}|$ are located in the corona, not in the blob. Therefore, for the most part of the simulation the peak of the adiabatic heating of the charged fluid takes place far from the blob.

In summary, the conclusion from this comparison is that the frictional heating is in general not negligible with respect to the adiabatic heating and that in certain regions of the domain (such as the borders of the falling blob) it is the main source of plasma heating according to our physical model.

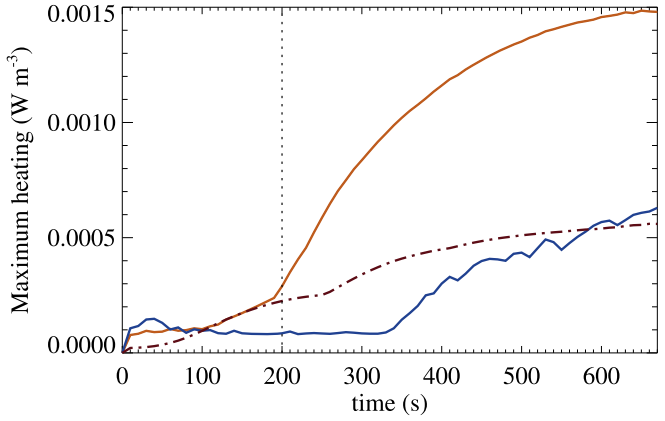

Figure A2. Maximum values of the heating terms as functions of time. Orange and blue solid lines correspond to the maximum values of the adiabatic heating of the charged and the neutral fluid, respectively. The dotted-dashed line represent the results for the frictional heating due to charged-neutral collisions. The vertical dotted line shows the time of the simulation represented in Figure A1.

ORCID iDs

David Martínez-Gómez https://orcid.org/0000-0002-2653-7020
Ramón Oliver https://orcid.org/0000-0003-4162-7240
Elena Khomenko https://orcid.org/0000-0003-3812-620X
Manuel Collados https://orcid.org/0000-0002-6210-9648

References

Ahn, K., Chae, J., Cho, K.-S., et al. 2014, SoPh, 289, 4117
Anan, T., Ichimoto, K., & Hillier, A. 2017, A&A, 601, A103
Antolin, P. 2020, PPCF, 62, 014016
Antolin, P., & Froment, C. 2022, FrASS, 9, 820116
Antolin, P., Martínez-Sykora, J., & Şahin, S. 2022, ApJL, 926, L29
Antolin, P., & Rouppevander Voort, L. 2012, ApJ, 745, 152
Antolin, P., Shibata, K., & Vissers, G. 2010, ApJ, 716, 154
Berenger, J.-P. 1994, JCoPh, 114, 185
Berger, T., Hillier, A., & Liu, W. 2017, ApJ, 850, 60
Draine, B. T. 1986, MNRAS, 220, 133
Field, G. 1965, ApJ, 142, 531
Froment, C., Auchère, F., Mikić, Z., et al. 2018, ApJ, 855, 52
Hillier, A. 2019, PhPl, 26, 082902
Hirayama, T. 1985, SoPh, 100, 415
Khomenko, E., Collados, M., & Díaz, A. 2016, ApJ, 823, 132
Khomenko, E., Collados, M., Díaz, A., & Vitas, N. 2014, PhPl, 21, 092901
Kohutova, P., Antolin, P., Popovas, A., & Szydlarski, M. 2020, A&A, 639, A20
Leake, J., Lukin, V., & Linton, M. 2013, PhPl, 20, 061202
Leake, J. E., Arber, T. D., & Khodachenko, M. L. 2005, A&A, 442, 1091
Li, X., Keppens, R., & Zhou, Y. 2022, ApJ, 926, 216
Martínez-Gómez, D., Oliver, R., Khomenko, E., & Collados, M. 2020, A&A, 634, A36
Martínez-Gómez, D., PopescuBraileanu, B., Khomenko, E., & Hunana, P. 2021, A&A, 650, A123
Martínez-Gómez, D., Soler, R., & Terradas, J. 2018, ApJ, 856, 16
Mendoza-Briceño, C., Sigalotti, L., & Erdélyi, R. 2005, ApJ, 624, 1080
Mikic, Z., Lionello, R., Mok, Y., Linker, J., & Winebarger, A. 2013, ApJ, 773, 94
Mok, Y., Mikic, Z., Lionello, R., Downs, C., & Linker, J. 2016, ApJ, 817, 15
Müller, D. A. N., DeGroof, A., Hansteen, V. H., & Peter, H. 2005, A&A, 436, 1067
Oliver, R., Soler, R., Terradas, J., & Zaqarashvili, T. V. 2016, ApJ, 818, 128
Oliver, R., Soler, R., Terradas, J., Zaqarashvili, T. V., & Khodachenko, M. L. 2014, ApJ, 784, 21
Parchevsky, K. V., & Kosovichev, A. G. 2009, ApJ, 694, 573
Parker, E. 1953, ApJ, 117, 431
Pereira, T. D., Voort, L., & Carlsson, M. 2016, ApJ, 824, 65
Popescu Braileanu, B., Lukin, V. S., Khomenko, E., & deVicente, A. 2019a, A&A, 630, A79
Popescu Braileanu, B., Lukin, V. S., Khomenko, E., & deVicente, A. 2019b, A&A, 627, A25
Popescu Braileanu, B., Lukin, V. S., Khomenko, E., & deVicente, A. 2021a, A&A, 646, A93
Popescu Braileanu, B., Lukin, V. S., Khomenko, E., & deVicente, A. 2021b, A&A, 650, A181
Schad, T. 2018, ApJ, 865, 31
Soler, R., Carbonell, M., Ballester, J. L., & Terradas, J. 2013, ApJ, 767, 171
Stellmacher, G., & Wiehr, E. 2017, SoPh, 292, 83
Wiehr, E., Stellmacher, G., Balthasar, H., & Bianda, M. 2021, ApJ, 920, 47
Wiehr, E., Stellmacher, G., & Bianda, M. 2019, ApJ, 873, 125
Xia, C., Keppens, R., & Fang, X. 2017, A&A, 603, A42
Zapiór, M., Heinzel, P., & Khomenko, E. 2022, ApJ, 934, 16
Zaqarashvili, T. V., Khodachenko, M. L., & Rucker, H. O. 2011, A&A, 529, A82
Zhang, F., Poedts, S., Lani, A., Kuźma, B., & Murawski, K. 2021, ApJ, 911, 119